Supplementary information

Piezotronic-probe modulates piezoelectric-electric-thermal coupling field in GaN power electronics

Zilong Dong[1,2,3,#], Yuxiu Liu[1,2,3,#], Wei Sha[1,2,3,#], Bingjun Wang[1,2,3], Ding Li[1,2], Yuxin Wang[1,2], Jiangwen Wang[1,2,3], Peiran Tian[1,2], Yong Long[1,2], Junyi Zhai[1,2,3,*], Weiguo Hu[1,2,3,*]

[1]Beijing Institute of Nanoenergy and Nanosystems, Chinese Academy of Sciences, Beijing, 101400, China

[2]School of Nanoscience and Technology, University of Chinese Academy of Sciences, Beijing 100049, China

[3]Huairou Laboratory, Beijing, 100049, China

[#]These authors contributed equally: Zilong Dong, Yuxiu Liu, Wei Sha

[*]e-mail: zhaijunyi@binn.cas.cn

[*]e-mail: huweiguo@binn.cas.cn

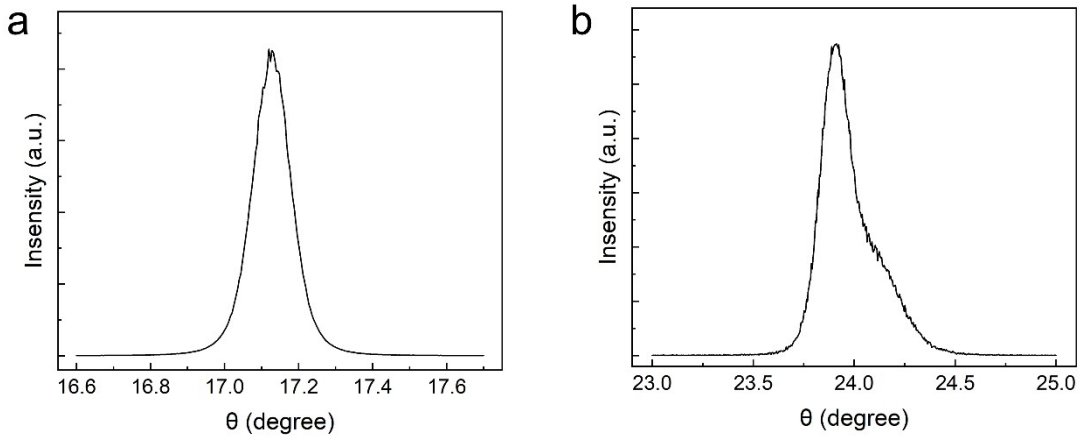

Fig. S1. (a) The rocking curve of the GaN (002) crystal plane. (b) The rocking curve of the GaN (102) crystal plane.

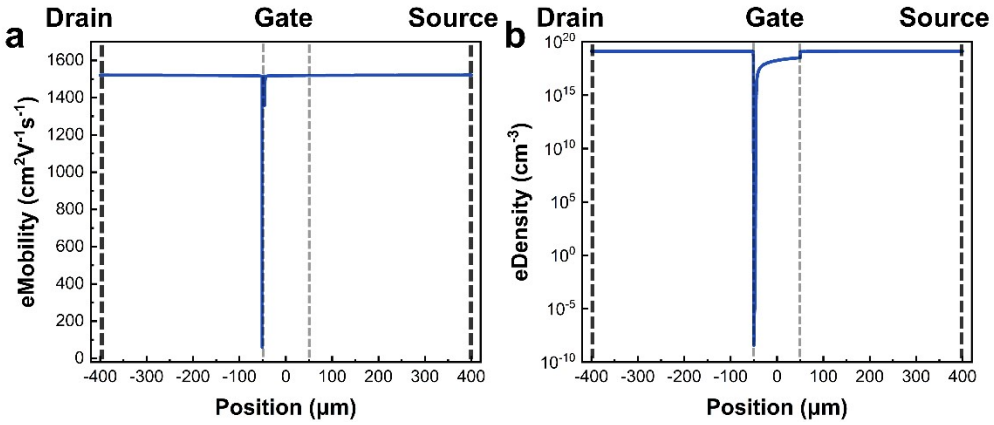

Fig. S2. (a) The distribution of simulated electron mobility along the channel direction. (b) The simulated electron density distribution along the channel direction.

Fig. S2 shows the distribution of electron mobility and electron density along the channel direction in simulation. It can be observed that the electron mobility decreases in the position of the large electric field, according to the high-field saturation mobility model (Canali model). Moreover, due to the depletion effect of the vertical large electric field, the 2DEG concentration decreases from greater than 10^{19} cm^{-3} to almost non-existent electrons. Furthermore, the marginal reduction of 2DEG concentration under the gate electrode can be attributed to the Schottky contact induced electron depletion.

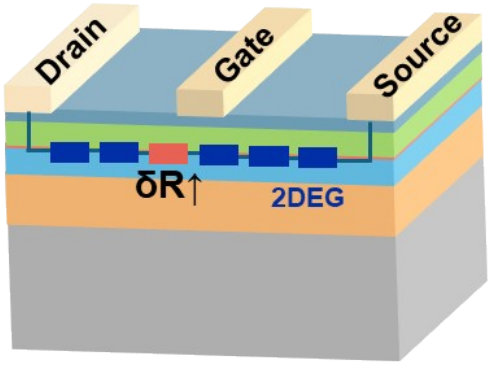

Fig. S3. Schematic diagram of a differential resistance model.

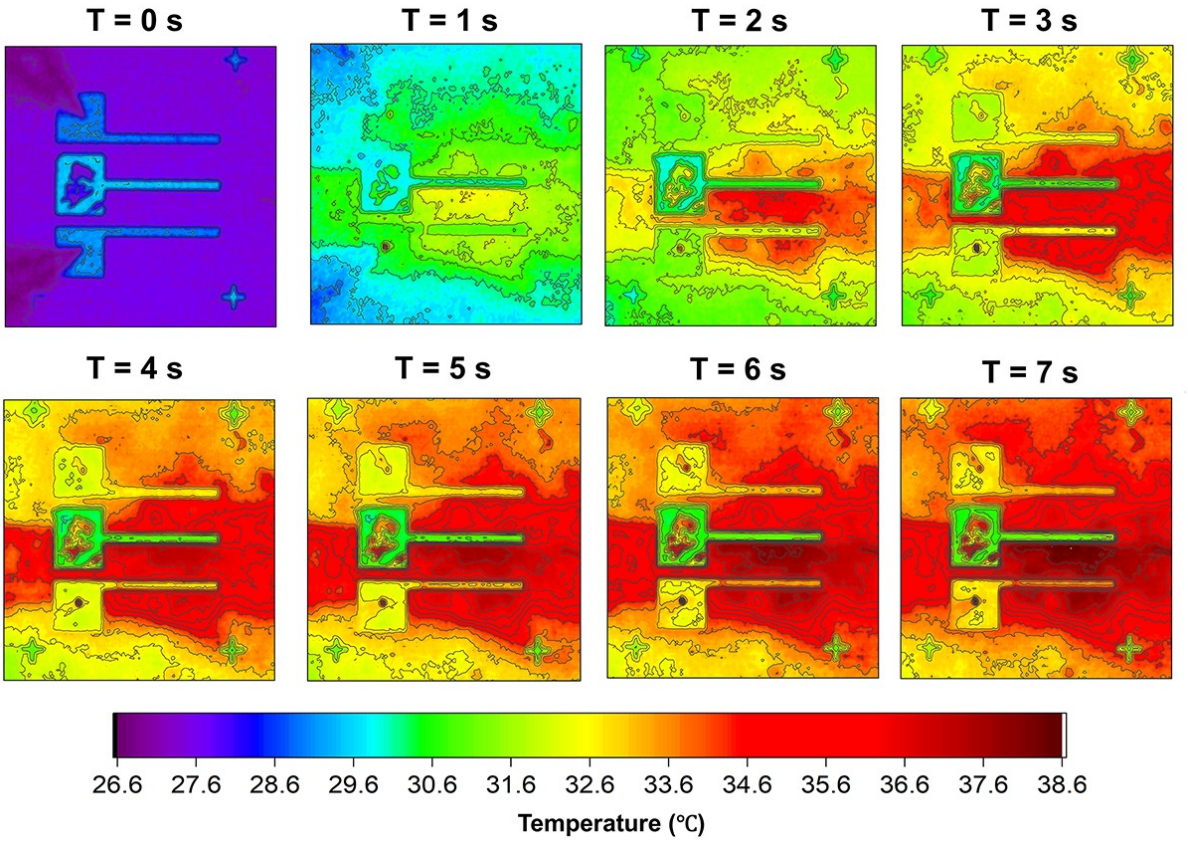

Fig. S4. The isotherm diagram of the GaN HEMT in 0-7 seconds after voltage application.

The equivalent transformation of parameters for Foster model and Cauer model:

The transient temperature curve of the device can be obtained by the Foster thermal network model and Cauer thermal network model, as shown in Fig. S5. The Foster model is simple in structure and easy to fit analytical formulas, while the parameters of Cauer model have practical physical significance. Therefore, it is important to convert the fitted Foster model parameters to Cauer model parameters. Since both two models represent the relationship between device temperature and time, the two models are mathematically equivalent. Their parameters can be equivalently transformed.

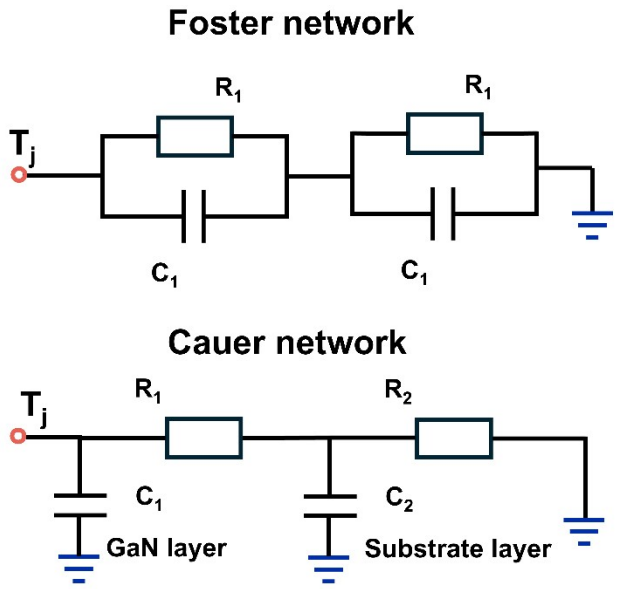

Fig. S5. Schematic of the Foster and Cauer network model.

In the complex frequency domain, the total thermal impedance of Foster network model is the sum of the thermal impedance of each node network, which is:

$$Z(s) = \sum_{i=1}^{n} \frac{R_i}{1 + sR_iC_i}$$

where $Z(s)$ represents the total thermal impedance, and R_i and C_i represent the thermal resistance and heat capacity of layer i, respectively. The impedance expression of a Cauer model is:

$$Z(s) = \cfrac{1}{sC_1 + \cfrac{1}{R_1 + \cfrac{1}{sC_2 + \cfrac{1}{R_2 + \cdots + \cfrac{1}{sC_n + \cfrac{1}{R_n}}}}}}$$

Since the Foster and Cauer model represent the same power device, the two model parameters can be converted into each other, and the conversion process is as follows.

Firstly, the expression of Foster model is converted to:

$$Z(s) = \frac{n_0 + n_1 s + \cdots + n_{N-1} s^{N-1}}{d_0 + d_1 s + \cdots + d_N s^N}$$

where the n_N and d_N are a linear combination of R_i and C_i of Foster model, by comparing the coefficients corresponding to the s^N after converting. In this case, the admittance $Y(s)$ of the network is $1/Z(s)$. For Cauer networks, the thermal resistance R_n and heat capacity C_n need to be extracted from the impedance $Z(s)$ or admittance $Y(s)$ of the device thermal network. According to the Cauer network model structure diagram shown in Fig. 3 (c), a parallel heat capacity should first be extracted after the heat source. Assuming parameter "s" approaches infinity, the heat capacity can be expressed as:

$$C_1 = \frac{1}{s} Y(s) \approx \frac{d_N}{n_{N-1}}$$

So, we get a heat capacity C_1, and then subtract this heat capacity from the total admittance $Y(s)$, and we get a new admittance $Y^{(1)}(s)$ that eliminates the s^N term:

$$Y^{(1)}(s) = Y(s) - \frac{d_N}{n_{N-1}} s = \frac{d_0^{(1)} + d_1^{(1)} s + \cdots + d_{N-1}^{(1)} s^{N-1}}{n_0 + n_1 s + \cdots + n_{N-1} s^{N-1}}$$

where $d^{(1)}$ is coefficient of s after subtracting the s^N term, using the combination of original d and n. The following $d^{(i)}$ and $n^{(i)}$ are represented in this way. Then, according to the new

admittance $Y^{(1)}(s)$, a new impedance is obtained by $Z^{(1)}(s)=1/\ Y^{(1)}(s)$. Then we continue to assume that s approaches infinity, and we get the thermal resistance R_1.

$$R_1 \approx \frac{n_{N-1}}{d_{N-1}^{(1)}}$$

Continue subtracting R_1 from $Z^{(1)}(s)$ to get a new $Z^{(2)}(s)$:

$$Z^{(2)}(s) = Z^{(1)}(s) - R_1 = \frac{n_0^{(1)} + n_1^{(1)}s + \cdots + n_{N-2}^{(1)}s^{N-2}}{d_0^{(1)} + d_1^{(1)}s + \cdots + d_{N-1}^{(1)}s^{N-1}}$$

According to the above calculation, a R_1 and C_1 of Cauer model are extracted, and the order of formula is reduced from s^{N-1} and s^N to s^{N-2} and s^{N-1}, and the thermal resistance and heat capacity of all Cauer networks can be obtained by continuing to deduce new R_n and C_n. At this time, R_n and C_n of the Cauer network are represented by the initial n_{N-1} and d_N, while n_{N-1} and d_N can be represented by C_i and R_i of the Foster network. In this way, we successfully link the thermal resistance and heat capacity of the Foster network and the Cauer network together and can convert to each other.

Repeatability and Error Testing

Regarding the repeatability and error range, we conducted repeatability tests to verify the effectiveness of the piezotronic-probe strategy. Firstly, we conducted 12 repeated measurements on a single device, and the temperature variation is shown in Fig. S6(a). During these 12 measurements, the temperature decreased approximately linearly under external stress, and the temperature variation under the same stress was relatively small. Fig. S6(b) presents the statistical results of the measurements. When the lifting height was 30 μm, the average temperature decreased from 45.9±0.26 ℃ to 43.6±0.28 ℃. The temperature rise (ΔT) decreased by 12.17±0.55%. The above results effectively demonstrate the repeatability of the piezotronic-probe strategy for individual devices.

For the repetitive results among multiple devices, we conducted multiple measurements on 15 devices, resulting in a total of 45 temperature variation curves. As shown in Fig. S6(c), the temperature of each measurement decreased approximately linearly under external stress. Due to the significant temperature differences between the devices, we conducted a statistical analysis on the decreasing ratio of the temperature rise (ΔT), as shown in Fig. S6(d). When the lifting height was 30 μm, the average temperature decreasing ratio was s 10.28±3.76%, the median was 9.66%. Due to the influence of the device manufacturing process, there are temperature differences between the devices, but there is still a noticeable temperature reduction. The temperature reduction trend of each device is similar, and the temperature reduction curves are approximately parallel from Fig. S6(c). This proves the effectiveness of the repetition between the devices.

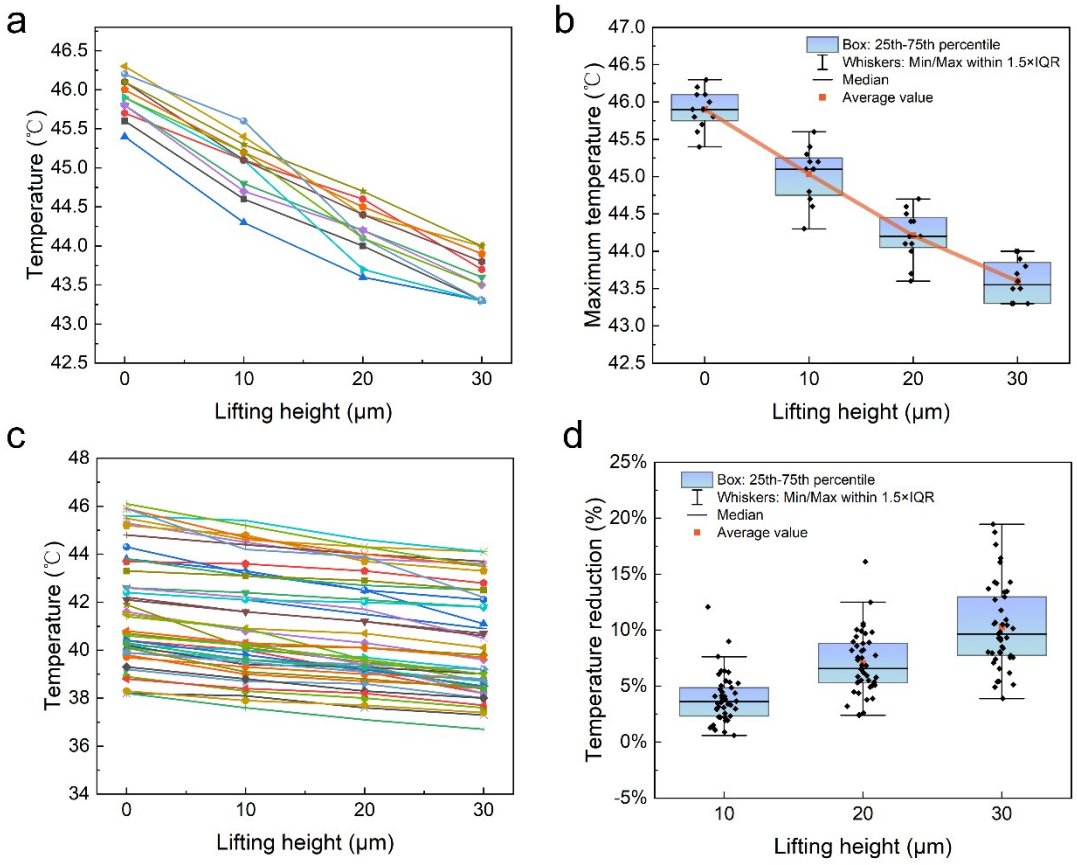

Fig. S6. (a) The results of 12 temperature measurements for a single device under different external stresses. (b) The statistical results of 12 temperature measurements of a single device under different external stresses. (c) The temperature changes of 15 devices were measured multiple times under different external stress conditions. (d) The statistical results of temperature reduction obtained from multiple measurements of 15 devices under different external stresses.

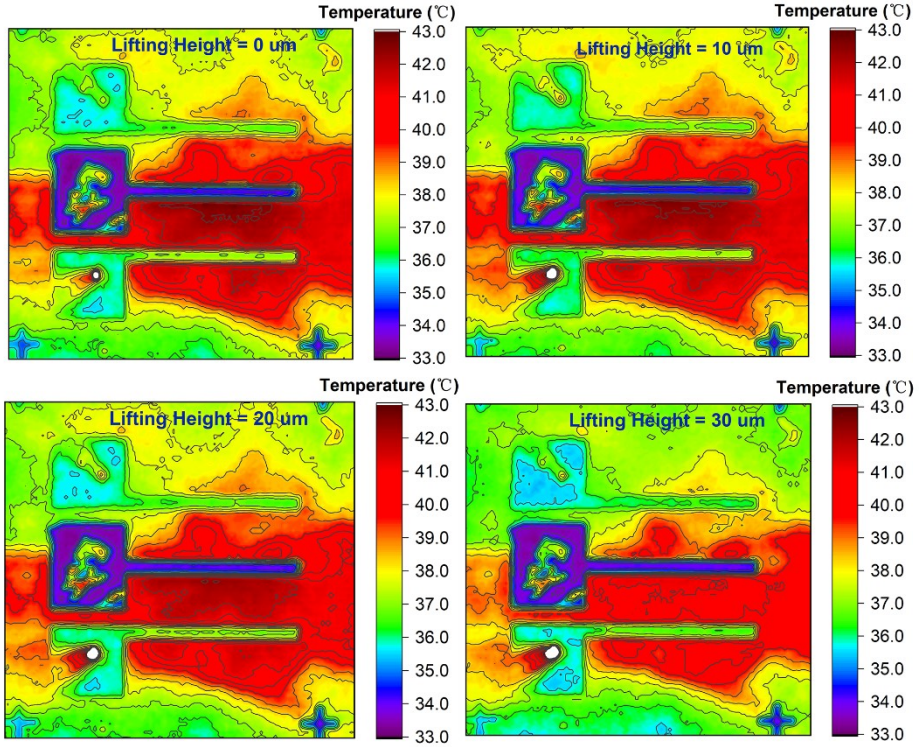

Fig. S7. The isotherm diagram of the GaN HEMT at different lifting heights. The temperature range and the represented colors of the four isotherms are consistent. It can be observed that as the lifting height increases, the temperature of the device decreases, and the diffusion area of temperature decreases.

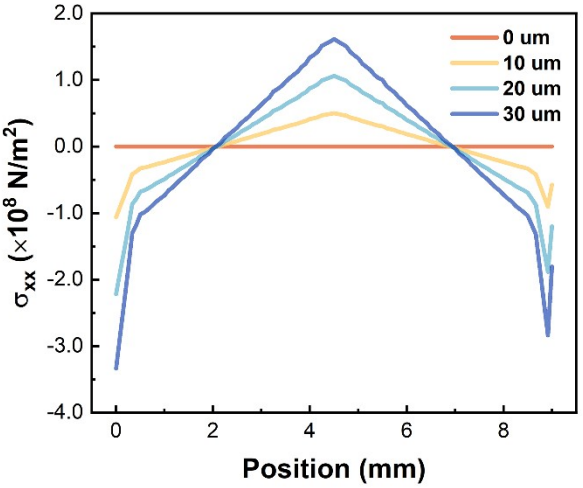

Fig. S8. The distribution of σ_{xx} along the channel direction at different lifting heights.

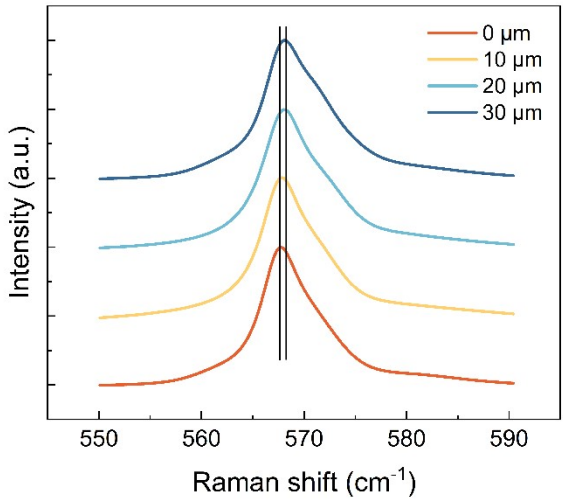

Fig. S9. Raman spectra with the lifting height of 0 - 30 μm.

Theoretical analysis

As illustrated in Fig. 6(b), external stress effectively modulates the depth of the triangular potential well at the heterointerface, which originates from the total polarization reduction induced by piezoelectric polarization change under external stress. The variation of the polarization vector component with the applied stress is as follows[1,2]:

$$\begin{bmatrix} P_x \\ P_y \\ P_z \end{bmatrix} = \begin{bmatrix} P_x^{sp} \\ P_y^{sp} \\ P_z^{sp} \end{bmatrix} + \begin{bmatrix} d_{11}\ d_{12}\ d_{13} \\ d_{21}\ d_{22}\ d_{23} \\ d_{31}\ d_{32}\ d_{33} \end{bmatrix} \begin{bmatrix} \sigma_{xx} \\ \sigma_{yy} \\ \sigma_{zz} \end{bmatrix}$$

where the P_α and P_α^{sp} is total polarization and spontaneous polarization, d_{ij} is the piezoelectric coefficients and $\sigma_{\alpha\alpha}$ is the stress, and α represent x, y and z directions.

The decrease in polarization intensity leads to the reduction in electron density, which can be obtained from the following formula: $q_{PE} = -\nabla \cdot \vec{P}$, where q_{PE} is polarization charge density, $\vec{P}$ is total polarization vector, and it can be converted into a 2DEG concentration (σ_{2DEG}).

Furthermore, the electrical characteristics of the device were simulated. The change rules of output, transfer characteristics and threshold voltage are consistent with the experimental results. This is mainly caused by the change in the 2DEG concentration, which can be obtained by the following model. Considering the one-dimensional simplified model, according to the current density equation, the source-drain current (I_{DS}) of 2DEG channel is[3]:

$$I_{DS} = eWv(x)\sigma_{2DEG}(x)$$

where W is gate width, $v(x)$ is the electron velocity along the channel and σ_{2DEG} is the concentration of 2DEG. The most simplified approximation of electron velocity is given in a two-stage model as follows[3]:

$$v(F) = \begin{cases} \mu F, & F < F_s \\ v_s, & F \geq F_s \end{cases}$$

$$F(x) = \frac{\mathrm{d}U(x)}{\mathrm{d}x}$$

μ is electron mobility, F is electric field and , F_s represents the electric field at which electron velocity saturates, v_s is saturation electron velocity and U is electric potential. Finally, the simulation was conducted to compare the device temperature under external stress. The results indicate that the application of external stress leads to a decrease in device temperature, as illustrated in Fig. 6(f). For power devices, the maximum junction temperature can be calculated by[4–6]:

$$\Delta T = T_j - T_a = P \cdot \sum_i R_{thi}$$

where ΔT, T_j and T_a are the rising temperature, the maximum junction temperature and the ambient temperature, P is thermal dissipation power of device and R_{thi} is the thermal resistance of the i-th thermal path, which can be obtained from the transient thermal test described in the above of this study. Summing the R_{thi} obtains the equivalent thermal resistance of the device from the maximum junction temperature position to the external environment. Combining the current calculations of the above, we can get the following formula:

$$T_j = T_a + eWv(x)\sigma_{2DEG}(x)U \cdot \sum_i R_{thi}$$

This formula reveals that device temperature can be effectively modulated via piezoelectric polarization as a bridging parameter. In addition, factors such as the source-drain voltage, gate width, electron saturation velocity, and device thermal resistance also play significant roles in influencing the device temperature. Herein, in the formula delineated above for calculating the thermal effects, the variation of the 2DEG concentration is attributed to the alteration of piezoelectric polarization field according to piezotronic effect, meanwhile, the electron saturation velocity and voltage distribution is related to electrical-field characteristics of device. Therefore, this formula successfully integrates piezotronics with electrothermal models to construct a piezoelectric-electric-thermal coupling model. This model provides theoretical foundation for our piezotronic-probe strategy, whereby the piezotronic-probe approach modulates the device's polarization field through external stress fields, subsequently regulating the thermal field via the 2DEG as a medium. Furthermore, this model elucidates the intricate piezoelectric-electric-thermal coupling interactions within the device, offering crucial guidance for performance optimization and development of advanced thermal management strategies.

Reference

1 C. Jiang, T. Liu, C. Du, X. Huang, M. Liu, Z. Zhao, L. Li, X. Pu, J. Zhai, W. Hu and Z. Lin Wang, *Nanotechnology*, 2017, **28**, 455203.

2 Y. Zhang, Y. Leng, M. Willatzen and B. Huang, *MRS Bull.*, 2018, **43**, 928–935.

3 P. P. Ruden, *IEEE Trans. Electron Devices*, 1990, **37**, 2267–2270.

4 Y. Zhang, H. Han, N. Wang, P. Zhang, Y. Fu, M. Murugesan, M. Edwards, K. Jeppson, S. Volz and J. Liu, *Adv. Funct. Mater.*, 2015, **25**, 4430–4435.

5 N. Sahebghalam, M. Shalchian, A. Chalechale and F. Jazaeri, *IEEE Trans. Electron Devices*, 2022, **69**, 4821–4827.

6 Z. Cheng, Z. Huang, J. Sun, J. Wang, T. Feng, K. Ohnishi, J. Liang, H. Amano and R. Huang, *Appl. Phys. Rev.*, DOI:10.1063/5.0185305.